



Investigation of the neutron distribution deformation by parity-violating electron scattering

Tongqi Liang ¹, Hongkai Wang,² Jian Liu ^{2,3,4,*} and Zhongzhou Ren^{1,5,†}

¹*School of Physics Science and Engineering, Tongji University, Shanghai 200092, China*

²*College of Science, China University of Petroleum (East China), Qingdao 266580, China*

³*Laboratory of High Precision Nuclear Spectroscopy, Institute of Modern Physics, Chinese Academy of Sciences, Lanzhou 730000, China*

⁴*Guangxi Key Laboratory of Nuclear Physics and Nuclear Technology, Guangxi Normal University, Guilin 541004, China*

⁵*Key Laboratory of Advanced Micro-Structure Materials, Ministry of Education, Shanghai 200092, China*



(Received 24 May 2023; accepted 21 June 2023; published 11 July 2023)

Parity-violating electron scattering (PVES) serves as an effective and model-independent method to investigate the spatial distributions of neutrons in nuclei. The existing PVES model assumes spherical neutron density distributions, while many nuclei show deformation. In this paper, we develop a deformed PVES model, which combines the deformed relativistic mean-field model and the distorted wave Born approximation, to evaluate how the deformation of the neutron density affects the parity-violating asymmetry A_{PV} . Our calculations demonstrate that the deformed PVES model is capable of recovering the A_{PV} results for spherical nuclei. Moreover, for deformed odd- A nuclei, the deformed PVES model provides larger A_{PV} calculations around the diffraction minima. These findings suggest that PVES can be used to extract the neutron deformation and construct a comprehensive understanding of the neutron structure in nuclei.

DOI: [10.1103/PhysRevC.108.014312](https://doi.org/10.1103/PhysRevC.108.014312)

I. INTRODUCTION

Parity-violating electron scattering (PVES) provides a crucial window for many significant topics, including investigations into the standard model, electroweak form factors of the nucleon, as well as the neutron distribution in nuclei [1]. The precise weak charge of the proton extracted by using PVES can determine the axial electron and vector quark weak coupling constants in the standard model and place important restrictions on new beyond-standard-model physics [2,3]. Combining the proton and neutron electromagnetic form factors, the neutral weak form factors measured by PVES allow the determination of the strange quark form factors [4–6]. Since Z^0 bosons, which mediate the weak interaction, couple primarily with neutrons at low four-momentum transfer squared Q^2 , PVES off nuclei provides a precise and model-independent way to shed light on the neutron density distribution in nuclei [7–13]. A thorough understanding of the neutron density distribution is essential for investigating neutron-excess systems spanning from exotic isotopes to macroscopically large objects, e.g., neutron stars [14–20].

Great progress has been made on PVES experiments off nuclei. The PREX-II experiment, carried out at Thomas Jefferson Lab (JLab), measured the parity-violating asymmetry $A_{PV} = 550 \pm 16(\text{stat}) \pm 8(\text{syst})$ parts per billion for ^{208}Pb . This measurement accurately determined the neutron skin $R_n - R_p = 0.283 \pm 0.071$ fm for ^{208}Pb and provided a stringent laboratory constraint on the symmetry energy of nuclear

matter [9,10]. The CREX experiment measured $A_{PV} = 2668 \pm 106(\text{stat}) \pm 40(\text{syst})$ parts per billion and provided the neutron skin $R_n - R_p = 0.121 \pm 0.026$ fm for ^{48}Ca , which can be compared with microscopic calculations from the basic nucleon-nucleon and three-nucleon forces [11,21]. Recently, to account for the background in the Q_{weak} experiment, A_{PV} of ^{27}Al was measured: $A_{PV} = 2.16 \pm 0.11(\text{stat}) \pm 0.16(\text{syst})$ parts per million [22]. It is also of particular interest on its own to extract the neutron skin of a light complex nucleus. As expected for ^{27}Al with one excess neutron, the corresponding neutron skin $R_n - R_p = -0.04 \pm 0.12$ fm is small, which can serve as a benchmark for determinations of the neutron skin by utilizing PVES on larger neutron-excess nuclei, e.g., ^{208}Pb .

The PVES experiment provides a highly anticipated observable and much theoretical effort has been made to clarify the relationship between the parity-violating asymmetry A_{PV} and nuclear properties. In the mean-field framework, it is revealed that the neutron skin can be extracted from the A_{PV} results by utilizing the high linear correlation between them [23]. Adopting chosen spherical neutron density profiles, such as the symmetrized two-parameter Fermi function, the overall neutron density profiles may be constrained with only two experimental measurements of A_{PV} [24]. In Ref. [25], the theoretical uncertainty was introduced for the first time to further investigate the current PVES model, and the correlations between A_{PV} and isovector nuclear properties were quantified in terms of the coefficient of determination (COD).

The nucleus is treated as spherically symmetric in the majority of PVES investigations, while most nuclei show deformations. The knowledge of nuclear deformation is essential for the emergence of drip lines, nuclear collective motions, heavy-ion collisions, and nucleosynthesis in stellar

*liujian@upc.edu.cn

†zren@tongji.edu.cn

environments [26–29]. It is also of particular interest that the isospin dependence of the nucleon-nucleon force may lead to different deformations of proton and neutron densities in some nuclei [30–32]. Therefore, a PVES model in the deformed framework is needed to take the deformations of proton and neutron densities into account. In Ref. [33], the Coulomb and weak multipole form factors of ^{27}Al were first evaluated with nonspherical nuclear density, in which the spherical part was obtained from the spherical relativistic mean field (RMF) model, and the deformed part was attributed to the $1d_{5/2}$ proton hole. The deformation of the neutron density was also taken into account because the proton hole is anticipated to polarize it.

In this paper, the deformed density distributions are generated by the axially deformed RMF model and expanded into various multipole density distributions. In the plane wave Born approximation (PWBA), multipole form factors are further calculated by the Fourier transformations of multipole density distributions. Coulomb distortions are taken into consideration by the distorted wave Born approximation (DWBA) to obtain accurate predictions of A_{PV} of heavy nuclei [34,35]. The combination of the axially deformed RMF model and the DWBA method is used to compute A_{PV} and is referred to as the deformed PVES model. With the deformed PVES model, we investigate A_{PV} of spherical nuclei ^{208}Pb and ^{48}Ca as well as deformed nuclei ^{27}Al and ^{133}Cs . The A_{PV} results from the spherical PVES model are also presented for comparison, in which the density distributions are from the spherical RMF model. By analyzing the A_{PV} results with and without neutron deformation, the impact of neutron deformation on A_{PV} is evaluated. The multipole form factors are also shown to investigate how neutron deformation influences A_{PV} , with a specific focus on the regions of diffraction minima where the neutron deformation effect is most pronounced. The deformed PVES model proposed in this paper may be helpful to investigate the deformed neutron density distribution in nuclei.

The rest parts are organized as follows. In Sec. II, the theoretical framework of the deformed PVES model is presented. In Sec. III, the parity-violating asymmetries are systematically investigated and the sensitivity of A_{PV} to the neutron deformation is discussed. Finally, a summary is given in Sec. IV.

II. THEORETICAL FRAMEWORK

In this section, the general deformed formalism for studying the parity-violating electron scattering is presented, in which the target nuclei are regarded as axially symmetric deformed rather than spherical. In this paper, we apply the deformed RMF model to calculate both the deformed proton and neutron density distributions. In the RMF model, the starting point is the effective Lagrangian [36]

$$\begin{aligned} \mathcal{L} = & \bar{\psi} \left\{ \gamma^\mu \left[i\partial_\mu - g_\omega \omega_\mu - \frac{g_\rho}{2} \vec{\tau} \cdot \vec{\rho}_\mu - \frac{e}{2} (1 + \tau^3) A_\mu \right] \right. \\ & \left. - (M - g_s \sigma) \right\} \psi \\ & + \frac{1}{2} \partial^\mu \sigma \partial_\mu \sigma - \frac{1}{2} m_\sigma^2 \sigma^2 - \frac{\kappa}{3!} (g_s \sigma)^3 - \frac{\lambda}{4!} (g_s \sigma)^4 \end{aligned}$$

$$\begin{aligned} & - \frac{1}{4} \Omega^{\mu\nu} \Omega_{\mu\nu} + \frac{1}{2} m_\omega^2 \omega^\mu \omega_\mu + \frac{\xi}{4!} (g_\omega^2 \omega^\mu \omega_\mu)^2 \\ & - \frac{1}{4} \vec{R}^{\mu\nu} \cdot \vec{R}_{\mu\nu} + \frac{1}{2} m_\rho^2 \vec{\rho}^\mu \cdot \vec{\rho}_\mu \\ & - \frac{1}{4} F^{\mu\nu} F_{\mu\nu} + U_{\text{eff}}(\omega_\mu, \vec{\rho}^\mu), \end{aligned} \quad (1)$$

where U_{eff} is the nonlinear $\omega - \rho$ term,

$$U_{\text{eff}}(\omega_\mu, \vec{\rho}^\mu) = \Lambda_v (g_\rho^2 \vec{\rho}^\mu \cdot \vec{\rho}_\mu) (g_\omega^2 \omega^\mu \omega_\mu). \quad (2)$$

With the Euler-Lagrange equation, one can derive the Dirac equations for nucleons and the Klein-Gordon equations for mesons. For axially deformed nuclei, the single-particle wave functions are expanded into eigenfunctions of an axially deformed harmonic oscillator. The motion equations, on the basis of the no-sea approximation and mean-field approximation, are iteratively solved, and the single-particle Dirac spinor can be written as

$$\psi_i(\mathbf{r}, t) = \begin{pmatrix} f_i(\mathbf{r}, s) \\ i g_i(\mathbf{r}, s) \end{pmatrix} \chi_{t_i}(t), \quad (3)$$

where $f_i(\mathbf{r}, s)$ and $g_i(\mathbf{r}, s)$ are the two-dimensional Dirac spinors for the single-particle state i , and $\chi_{t_i}(t)$ represents the isospin function. The deformed neutron density $\rho_n(\mathbf{r})$ and proton density $\rho_p(\mathbf{r})$ are expressed as the sum of the contributions from the corresponding single-particle states. With $\rho_n(\mathbf{r})$ and $\rho_p(\mathbf{r})$, the deformed weak charge density distribution $\rho_W(\mathbf{r})$ can be written as [34]

$$\begin{aligned} \rho_W(\mathbf{r}) &= \int d^3 r' G_E(|\mathbf{r} - \mathbf{r}'|) [(1 - 4 \sin^2 \theta_W) \rho_p(\mathbf{r}') - \rho_n(\mathbf{r}')] \\ &= (1 - 4 \sin^2 \theta_W) \rho_C(\mathbf{r}) - \int d^3 r' G_E(|\mathbf{r} - \mathbf{r}'|) \rho_n(\mathbf{r}'), \end{aligned} \quad (4)$$

where $G_E(r) = \frac{Q^2}{8\pi} e^{-Qr}$ is the electric form factor of the single proton with $Q = 842.61$ MeV, and the weak mixing angle $\sin^2 \theta_W = 0.23$. $\rho_C(\mathbf{r}) = \int d^3 r' G_E(|\mathbf{r} - \mathbf{r}'|) \rho_p(\mathbf{r}')$ is the charge density distribution, where the neutron electric form factor is neglected. These densities are normalized, $\int d^3 r \rho_C(\mathbf{r}) = Z$ and $\int d^3 r \rho_W(\mathbf{r}) = Q_W$, with Z and $Q_W = Z(1 - 4 \sin^2 \theta_W) - N$ being the charge and weak charge numbers, respectively.

We expand the axially deformed charge and weak charge densities $\rho(r_\perp, z)$ in cylindrical coordinates with the Legendre function

$$\begin{aligned} \rho(r_\perp, z) &= \sum_\lambda \rho_\lambda(r) P_\lambda(\cos \theta) \\ &= \rho_0(r) + \rho_2(r) P_2(\cos \theta) + \dots, \end{aligned} \quad (5)$$

where the multipole component $\rho_\lambda(r)$ in spherical coordinates is written as

$$\rho_\lambda(r) = \frac{2\lambda + 1}{2} \int_{-1}^1 P_\lambda(\cos \theta) \rho(r_\perp, z) d(\cos \theta). \quad (6)$$

In the following, we present the formulas to calculate the parity-violating asymmetry A_{PV} in a deformed framework utilizing the above charge and weak charge density multipoles.

A_{PV} is defined as

$$A_{PV} = \frac{\sigma^+ - \sigma^-}{\sigma^+ + \sigma^-}, \quad (7)$$

where $\sigma^{+(-)}$ represents the differential cross section of longitudinally polarized electrons off unpolarized targets, with $+(-)$ corresponding to the spin of electrons parallel (antiparallel) to their momenta. In the frame of PWBA and considering the same proton and neutron densities, the parity-violating asymmetry A_{PV} can be written in the form [7]

$$A_{PV} = A_{PV}^0 = -\frac{G_F q^2 Q_W}{4\pi\alpha\sqrt{2}Z}. \quad (8)$$

Here $G_F = 1.16639 \times 10^{-5} \text{ GeV}^{-2}$ is the Fermi constant, $q = |\mathbf{q}|$ is the three-momentum transfer, and α is the fine structure constant. A_{PV}^0 is simply proportional to q^2 and contains no information on nuclear structures. Incorporating different proton and neutron densities, A_{PV} in PWBA becomes

$$A_{PV} = A_{PV}^0 \frac{W^{PV}(q)}{F^2(q)}. \quad (9)$$

The nuclear structure information is embedded in the ratio of the parity-violating response $W^{PV}(q)$ to the parity-conserving form factor $F^2(q)$. By decomposing them in a Rosenbluth expansion and only considering the longitudinal form factor for the forward scattering angles, $F^2(q)$ and $W^{PV}(q)$ can be expressed as the familiar Coulomb multipole form factor $F_{C\lambda}(q)$ and weak multipole form factor $F_{W\lambda}(q)$ [37]:

$$F^2(q) = \sum_{\lambda=0,2,\dots}^{2J} F_{C\lambda}(q)^2, \quad (10)$$

$$W^{PV}(q) = \sum_{\lambda=0,2,\dots}^{2J} F_{C\lambda}(q)F_{W\lambda}(q), \quad (11)$$

where J is the angular momentum of the nuclear ground state. Only even- λ terms remain because of the parity and time reversal invariance. The weak multipole form factor $F_{W\lambda}(q)$ can be expressed in terms of intrinsic form factor $\mathcal{F}_{W\lambda}(q)$ weighted by the Clebsch-Gordan coefficient

$$F_{W\lambda} = \langle Jk\lambda 0 | J\lambda Jk \rangle \mathcal{F}_{W\lambda}, \quad (12)$$

where k is the J projection along the nuclear symmetry axis. For $\lambda = 0$, the intrinsic multipole is contributed by the spherical part $\rho_{W0}(r)$ of the intrinsic weak charge density

$$\mathcal{F}_{W0}(q) = \frac{4\pi}{Q_W} \int r^2 \rho_{W0}(r) j_0(qr) dr, \quad (13)$$

where $j_0(qr)$ is the zeroth-order spherical Bessel function. Higher intrinsic multipoles ($\lambda \geq 2$) reflect the contributions of the deformed parts of the intrinsic weak charge density

$$\mathcal{F}_{W\lambda}(q) = \frac{4\pi}{Q_W \sqrt{2\lambda + 1}} \int r^2 \rho_{W\lambda}(r) j_\lambda(qr) dr, \quad (14)$$

where $\rho_{W\lambda}(r)$ is the λ_{th} multipole of the deformed intrinsic weak charge density, and $j_\lambda(qr)$ is the λ_{th} -order spherical Bessel function. Similarly, the Coulomb multipole form factors $F_{C\lambda}(q)$ can also be written in terms of the intrinsic form

factors $\mathcal{F}_{C\lambda}(q)$, which are related to the multipole intrinsic charge densities [38].

Combining Eqs. (9)–(14), one can obtain the form under the plane-wave description of the parity-violating asymmetry A_{PV} ,

$$\begin{aligned} A_{PV} &\approx A_{PV}^0 \frac{F_{C0}F_{W0} + F_{C2}F_{W2}}{F_{C0}^2 + F_{C2}^2} \\ &= \frac{A_{PV}^0 \frac{F_{C0}F_{W0}}{F_{C0}^2} + A_{PV}^0 F_{C2}F_{W2}}{F_{C0}^2 + F_{C2}^2}. \end{aligned} \quad (15)$$

$F_{C0}(F_{W0})$ dominates the A_{PV} results, except for the regions near the diffraction minima, where $F_{C2}(F_{W2})$ is significant. The contributions from higher multipoles ($\lambda > 2$) are small. Detail discussions can be found in Refs. [33,39,40]. Therefore, in this paper, we only consider the multipole form factors up to $\lambda = 2$. The PWBA method provides a powerful tool for the multipole analysis of form factors. However, the nuclear Coulomb distortion effects, being important near diffraction minima, are not considered in PWBA. In the above equation, we separate $A_{PV}^0 \frac{F_{C0}F_{W0}}{F_{C0}^2}$ out in the numerator, which is the parity-violating asymmetry with spherical density distributions. To obtain accurate quantitative results, we incorporate the Coulomb distortions for $A_{PV}^0 \frac{F_{C0}F_{W0}}{F_{C0}^2}$ by utilizing the DWBA method, and Eq. (15) can be rewritten as [33]

$$A_{PV} = \frac{A_{PV}^{\text{DW}} F_{C0}^2|_{\text{DW}} + A_{PV}^0 F_{C2}F_{W2}}{F_{C0}^2|_{\text{DW}} + F_{C2}^2}. \quad (16)$$

$A_{PV}^0 \frac{F_{C0}F_{W0}}{F_{C0}^2}$ in Eq. (15) is replaced by $A_{PV}^{\text{DW}} = \frac{\sigma^+|_{\text{DW}} - \sigma^-|_{\text{DW}}}{\sigma^+|_{\text{DW}} + \sigma^-|_{\text{DW}}}$, in which the cross section $\sigma^{+(-)}|_{\text{DW}}$ is calculated with the spherical charge and weak charge densities by the DWBA method. $F_{C0}|_{\text{DW}}$ is referred to as the zeroth-order Coulomb form factor including Coulomb distortion effects.

III. NUMERICAL RESULTS

In this section, the deformed PVES model given in Sec. II, which merges the deformed RMF model and the DWBA method, is applied to investigate the parity-violating asymmetry A_{PV} for both the spherical and deformed nuclei. The A_{PV} results from the spherical PVES model are also presented for comparison, which only contains $F_{C0}(q)$ and $F_{W0}(q)$ with density distributions from the spherical RMF model. By contrasting the spherical and deformed calculations, one can validate the deformed PVES model and investigate the effects of neutron deformation on PVES. In this paper, we place our focus on the results of weak charge densities $\rho_W(\mathbf{r})$, since the charge densities $\rho_C(\mathbf{r})$ have been investigated extensively [41–44].

A. Spherical nuclei

First, we investigate the parity-violating asymmetry A_{PV} of spherical nuclei ^{208}Pb and ^{48}Ca . Through the years, strong correlations have been found between the neutron skin of ^{208}Pb and the slope of the symmetry energy. The proton density can be extracted from the elastic electron scattering. Therefore, it is of particular interest to study the neutron

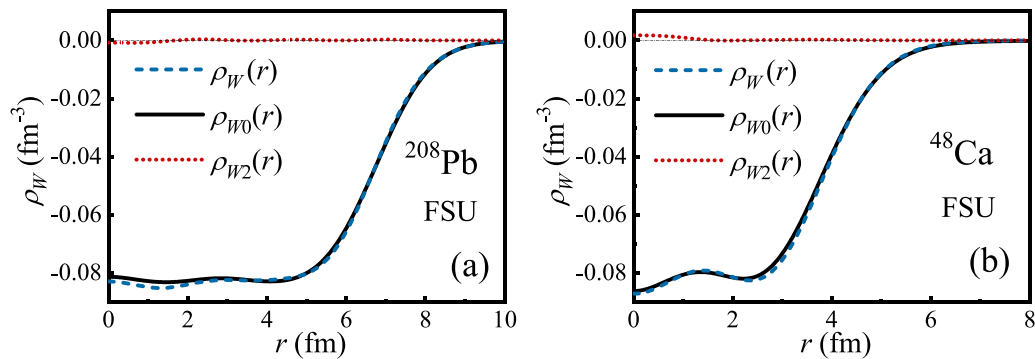


FIG. 1. (a) Weak charge density distributions of ^{208}Pb . The multipole weak charge density distributions $\rho_{W0}(r)$ and $\rho_{W2}(r)$ (solid line and dotted line) as well as the spherical density distribution $\rho_W(r)$ (dashed line) are respectively calculated by the deformed and spherical RMF models with the FSU parameter set. (b) Same as (a), but for ^{48}Ca .

density of ^{208}Pb utilizing parity-violating electron scattering. As a lighter double magic nucleus, it is more feasible to obtain the nuclear structure of ^{48}Ca in a microscopic calculation [21]. There has been an increasing interest in studying the parity-violating asymmetry of ^{48}Ca . The experimental A_{PV} results of ^{208}Pb and ^{48}Ca have been measured in the PREX-II and CREX experiments, respectively.

In Fig. 1(a), we present the multipole weak charge density distributions $\rho_{W0}(r)$ and $\rho_{W2}(r)$ of ^{208}Pb from the deformed RMF model. For comparison, the spherical density distribution $\rho_W(r)$ from the spherical RMF model is also shown. The precisely calibrated FSUGold (or “FSU”, for short) parametrization, which provides a modest neutron skin, is used to present predictions [23,36]. Inspecting the figure, the quadrupole density distribution $\rho_{W2}(r)$ is very close to zero. The results of the spherical part $\rho_{W0}(r)$ from the deformed RMF model are almost identical to $\rho_W(r)$ from the spherical RMF model; that is, for the spherical nucleus ^{208}Pb , the deformed RMF model can replicate the results of the spherical counterpart. The weak charge density distributions of ^{48}Ca are shown in Fig. 1(b), obtained from both the spherical and deformed RMF models. For ^{48}Ca , the results of $\rho_{W0}(r)$ from the deformed RMF model are also similar to $\rho_W(r)$ from the spherical RMF model.

According to Eqs. (9)–(11), for an even-even nucleus, only $F_{\text{C}0}(q)$ and $F_{\text{W}0}(q)$, which arise from the spherical portions of the deformed densities, contribute to the parity-violating asymmetry A_{PV} . With $\rho_{W0}(r)$ from the deformed RMF model, the A_{PV} results of ^{208}Pb are calculated and shown in Fig. 2(a) at the beam energy of 953 MeV, which is the energy of the PREX-II experiment. The A_{PV} results from the spherical PVES model and A_{PV}^0 in Eq. (8) are also displayed in the same figure for comparison. It is evident that the A_{PV} calculations from the spherical and deformed PVES models conform with the experimental data and coincide with each other in a large range of scattering angles ($\theta < 10^\circ$). When the same proton and neutron densities are fixed, the PWBA outcomes simply exhibit a q^2 behavior, i.e., the results of A_{PV}^0 , as shown in Eq. (8). The diffraction minima originate from the Coulomb distortion effects and the distinction between the proton and neutron densities [45]. The deformed PVES model incorporates the Coulomb distortion effects by the DWBA

and employs the different proton and neutron densities from the deformed RMF model. The spherical PVES model shares the same situation. Consequently, both the spherical and deformed PVES models demonstrate diffraction minima in the A_{PV} results.

With the density distributions in Fig. 1(b), the A_{PV} results of ^{48}Ca at the beam energy of 2180 MeV, corresponding to the energy of the CREX experiment, are also presented in Fig. 2(b). It can be seen that the A_{PV} results from both the deformed and spherical PVES models coincide with the experimental data, and the two theoretical results are practically the same. Combining the results of ^{208}Pb and ^{48}Ca , it can be concluded that, in the case of the spherical nuclei, the spherical and deformed RMF models provide essentially identical charge and weak charge density distributions. The A_{PV} results from the spherical PVES model can be reproduced using the deformed one. These findings provide nontrivial evidence of the validity of the deformed PVES model, which inspires us to further investigate the charge and weak charge density distributions for deformed nuclei.

B. Deformed nuclei

In addition to ^{208}Pb and ^{48}Ca , we also investigate the parity-violating electron scattering of ^{27}Al with the deformed PVES model. The PVES experiment of ^{27}Al was performed at JLab. The angular momentum of ^{27}Al is $J^\pi = 5/2^+$, and, according to Eqs. (9)–(11), A_{PV} contains higher multipole form factors, which correspond to the deformed parts of $\rho_W(\mathbf{r})$ and $\rho_C(\mathbf{r})$.

In deformed RMF calculations with the FSU parameter set, ^{27}Al has an oblate shape with the deformations $\beta_2^n = -0.324$ for the neutron density $\rho_n(\mathbf{r})$ and $\beta_2^p = -0.322$ for the proton density $\rho_p(\mathbf{r})$. Figure 3(a) displays the deformed neutron density of ^{27}Al from the deformed RMF model. Figure 3(b) presents the multipole weak charge density distributions $\rho_{W0}(r)$ and $\rho_{W2}(r)$, along with the spherical density distribution $\rho_W(r)$ from the spherical RMF model. The inset in Fig. 3(b) depicts the profile of the quadrupole density $\rho_{W2}(r)P_2(\cos\theta)$ in Eq. (5). It can be seen that $\rho_{W2}(r)P_2(\cos\theta)$ exhibits positive values in the x direction and negative values in the z direction, which lead to the oblate shape of ^{27}Al .

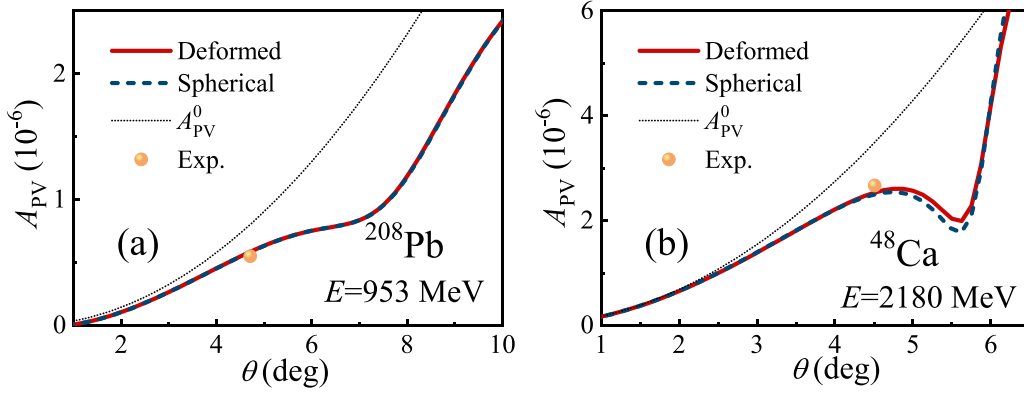


FIG. 2. (a) Parity-violating asymmetry A_{PV} of ^{208}Pb at the beam energy of 953 MeV versus the scattering angle. The dotted line shows the A_{PV}^0 results from PWBA. The solid line and dashed line represent the A_{PV} results from the deformed and spherical PVES models, respectively. The experimental value of A_{PV} is extracted from the PREX-II experiment [9]. (b) Same as (a), but for ^{48}Ca at the beam energy of 2180 MeV with the experimental value of A_{PV} extracted from the CREX experiment [11].

Moreover, it is well known that the nuclear deformation can alter the occupation numbers of the single-particle states, partially emptying states below the Fermi level and filling states above the Fermi level [46]. Concerning ^{27}Al , the $2s_{1/2}$ orbit is located above the neutron Fermi level $1d_{5/2}$. As shown in Fig. 3(b), since the nuclear deformation induces occupation of the $2s_{1/2}$ orbit, one can observe the enhancement of the central density for $\rho_{W0}(r)$ from the deformed RMF model.

With the multipole densities in Fig. 3(b), the A_{PV} results calculated by the deformed PVES model are presented in Fig. 4. To investigate the effects of neutron deformation on A_{PV} , the theoretical results with and without the quadrupole neutron density ρ_{n2} are offered for comparison. Recall that, in this paper, the quadrupole proton density ρ_{p2} is incorporated for all the A_{PV} results from the deformed PVES model. We also present the A_{PV} results from the spherical PVES model in the same figure. At small angles ($\theta < 9^\circ$), the effects of neutron deformation are not significant. Theoretical results are indistinguishable and coincide with the experimental data. As the scattering angle increases, theoretical results separate from each other. Especially at the diffraction minimum ($\theta \approx 13.5^\circ$), compared with the spherical calculations, the

A_{PV} results from the deformed PVES model with ρ_{n2} are located in the upper part and those excluding ρ_{n2} are located in the lower part. In deformed RMF calculations with the FSU parameter set, there is shape coexistence and there is a prolate solution for ^{27}Al , whose binding energy is slightly higher than that of the oblate solution. The corresponding A_{PV} results indicate a pattern similar to Fig. 4. Specifically, when compared to the spherical PVES model, the deformed PVES model with ρ_{n2} yields larger A_{PV} at the diffraction minimum, while the deformed PVES model without ρ_{n2} provides smaller A_{PV} .

The information regarding the difference between the proton and neutron densities can also be obtained from Fig. 4. In the deformed RMF calculations, when excluding ρ_{n2} , the neutron density is spherical and differs significantly from the deformed proton density. It leads to an obvious minimum of the A_{PV} results. When both ρ_{p2} and ρ_{n2} are considered, ^{27}Al exhibits similar proton and neutron densities in the deformed RMF model. Therefore, A_{PV} with ρ_{n2} exhibits a flatter pattern that is closer to A_{PV}^0 . These discussions suggest that the neutron deformation plays a significant role in the parity-violating asymmetries.

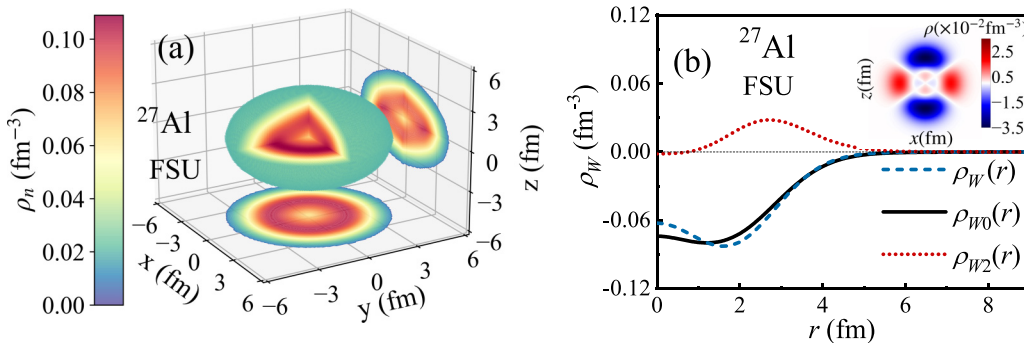


FIG. 3. (a) Deformed neutron density of ^{27}Al calculated from the deformed RMF model with the FSU parameter set. (b) Multipole weak charge density distributions $\rho_{W0}(r)$ and $\rho_{W2}(r)$ (solid line and dotted line) as well as the spherical density distribution $\rho_W(r)$ (dashed line), calculated by the deformed and spherical RMF models with the FSU parameter set. The inset is the profile of the quadrupole density $\rho_{W2}(r)P_2(\cos\theta)$ in Eq. (5).

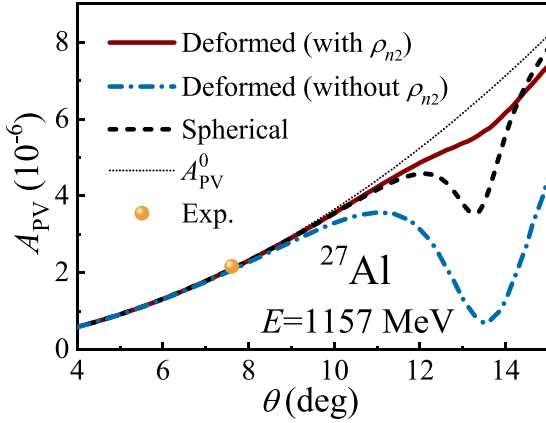


FIG. 4. Parity-violating asymmetry A_{PV} of ^{27}Al at the beam energy of 1157 MeV versus the scattering angle θ , where the densities are calculated from the spherical and deformed RMF models with the FSU parameter set. The solid line represents the A_{PV} results from the deformed PVES model, which includes the quadrupole neutron density ρ_{n2} from the deformed RMF model, while the dash-dotted line excludes ρ_{n2} . The quadrupole proton density ρ_{p2} is considered in the above two A_{PV} results from the deformed PVES model. The dashed line is the A_{PV} results from the spherical PVES model. The dotted line shows the A_{PV}^0 results from PWBA. The experimental value of A_{PV} is taken from Ref. [22].

The form factors are directly related to A_{PV} in Eq. (9) and are the Fourier transforms of the multipole densities. We discuss the form factors in the following to clarify how the neutron deformation influences A_{PV} . In Fig. 5, we present the quadrupole Coulomb form factor $F_{C2}(q)$ as well as the quadrupole weak form factors $F_{W2}(q)$ with and without the quadrupole neutron density ρ_{n2} . In the case without ρ_{n2} , $F_{W2}(q)$, which is fully contributed by the quadrupole proton density ρ_{p2} , is tiny due to the small weak charge of the proton. Therefore the impact arising from the deformed density parts is primarily reflected in the contribution of $F_{C2}(q)$,

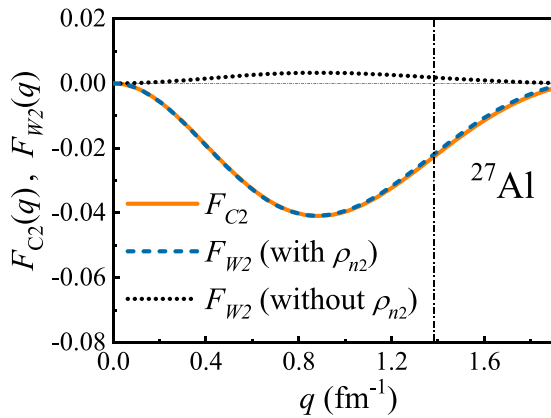


FIG. 5. Quadrupole Coulomb form factor $F_{C2}(q)$ (solid line) as well as quadrupole weak form factors $F_{W2}(q)$ with (dashed line) and without (dotted line) the quadrupole neutron density ρ_{n2} . The vertical dash-dotted line delineates the location of the diffraction minimum in Fig. 4.

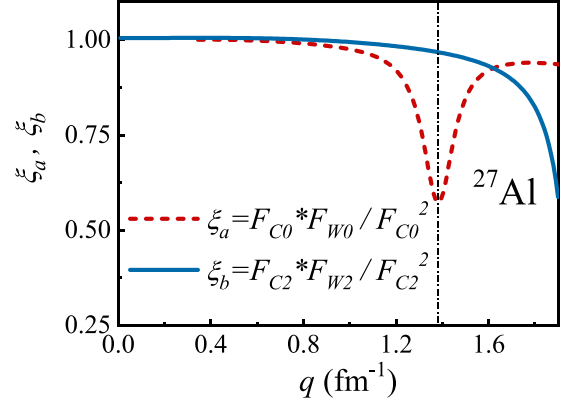


FIG. 6. Ratios of form factors. Both the quadrupole proton density ρ_{p2} and the quadrupole neutron density ρ_{n2} are contained in $F_{C2}(q)$ and $F_{W2}(q)$. The vertical dash-dotted line delineates the location of the diffraction minimum in Fig. 4.

which increases the denominator of Eq. (15) and reduces A_{PV} throughout the whole region.

When ρ_{n2} is considered, the deformed proton and neutron densities are comparable. Therefore, $F_{C2}(q)$ and $F_{W2}(q)$ are very close to each other, as shown in Fig. 5. This leads to the complexity in evaluating the variation of A_{PV} results. We rewrite Eq. (15) as

$$A_{PV} = A_{PV}^0 \frac{F_{C0}F_{W0}}{F_{C0}^2} + A_{PV}^0 \frac{(\xi_b - \xi_a)F_{C2}^2}{F_{C0}^2 + F_{C2}^2}, \quad (17)$$

where $\xi_a = \frac{F_{C0}F_{W0}}{F_{C0}^2}$ and $\xi_b = \frac{F_{C2}F_{W2}}{F_{C2}^2}$ are the ratios of form factors. In Eq. (17), the contribution arising from the spherical density distribution is incorporated in the first term $A_{PV}^0 \frac{F_{C0}F_{W0}}{F_{C0}^2}$ and the deformed effect is included in the second term. The variation of A_{PV} depends on the magnitude relationship between ξ_a and ξ_b . The results of ξ_a and ξ_b are presented in Fig. 6, in which ρ_{n2} is included. It should be mentioned that $F_{W2}(q)$ and $F_{C2}(q)$ are calculated by the PWBA method, while $F_{W0}(q)$ and $F_{C0}(q)$ are evaluated by the DWBA method. At small momentum transfers $q < 0.8 \text{ fm}^{-1}$, ξ_a and ξ_b are almost

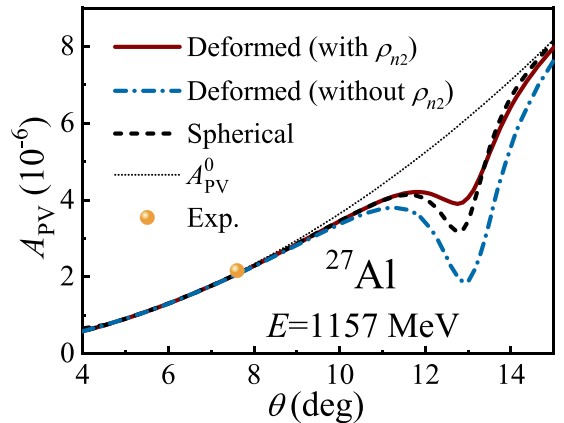
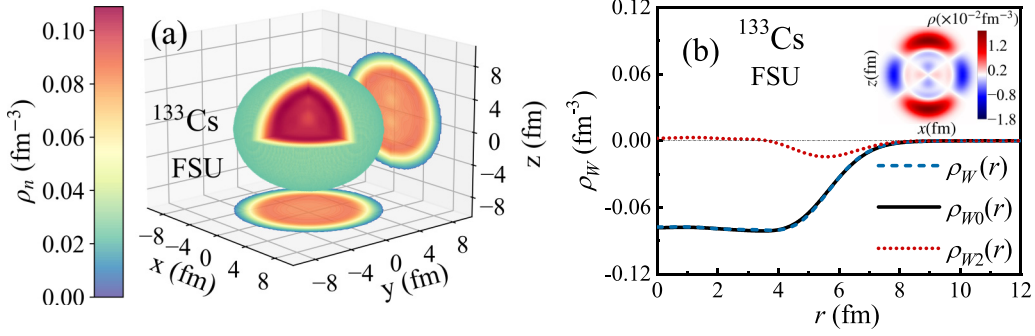


FIG. 7. Same as Fig. 4, but with the density distributions calculated from the spherical and deformed RMF models with the TM2 parameter set.


 FIG. 8. Same as Fig. 3, but for ^{133}Cs .

equal to 1. As the momentum transfer increases, ξ_a decreases faster than ξ_b . At the diffraction minimum $q \approx 1.38 \text{ fm}^{-1}$, $\xi_a = 0.57$ and $\xi_b = 0.97$. Substituting them into Eq. (17), the second term, which reflects the deformed effect, is positive and consequently increases A_{PV} , while in the region where ξ_a is larger than ξ_b , e.g., $q \approx 1.75 \text{ fm}^{-1}$, the second term decreases A_{PV} . It can also be seen from Eq. (17) that A_{PV} is a monotonically increasing function of $F_{W2}(q)$. With this relationship, one can link ρ_{n2} and A_{PV} .

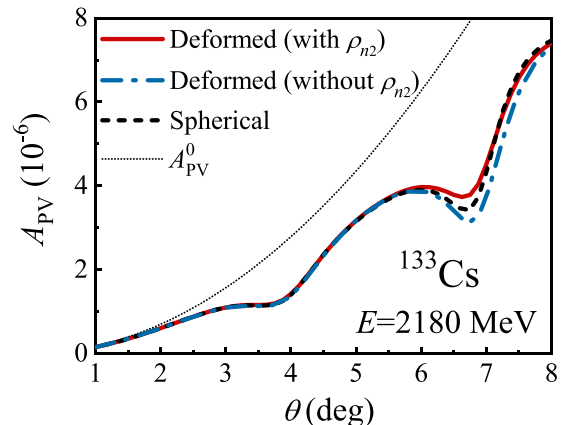
In the above discussions with the density distributions calculated by the RMF model with the FSU parameter set, it is found that ρ_{n2} has an important influence on A_{PV} . This general conclusion is applicable to the results of other RMF parameter sets as well. For brevity, we take the TM2 parameter set [47] as an example, and the corresponding A_{PV} results are shown in Fig. 7. The deformed RMF model with the TM2 parameter set provides a prolate shape for ^{27}Al with the deformations $\beta_2^n = 0.158$ for $\rho_n(\mathbf{r})$ and $\beta_2^p = 0.178$ for $\rho_p(\mathbf{r})$. It can be seen in Fig. 7 that the deformed PVES model with ρ_{n2} offers larger A_{PV} at the diffraction minimum in comparison to the spherical PVES model, while the deformed PVES model without ρ_{n2} provides smaller A_{PV} . The A_{PV} results in Figs. 4 and 7 for different RMF parameter sets are in agreement.

Nuclear deformation is very important for investigating the properties of the nuclear ground states [48,49]. The proton deformation has been extensively investigated by the data on electric properties. However, probing the neutron deformation is still enormously challenging, and the distinction between the deformations of proton and neutron densities has been suggested theoretically and experimentally [30–32]. Combining Figs. 4–7, we find that the deformed neutron structure of ^{27}Al can be investigated by the PVES experiment. One can extract the quadrupole weak form factor $F_{W2}(q)$ and constrain the neutron deformation with the experimental A_{PV} data at large scattering angles ($\theta = 12^\circ\text{--}14^\circ$). In Ref. [24], the authors demonstrated that the overall spherical weak charge density of ^{208}Pb can be constrained with the measurements of the weak form factor at two different momentum transfers. Inspired by this, a comprehensive understanding of the deformed neutron structure of ^{27}Al may be accessible with the help of the experimental values of A_{PV} at several chosen momentum transfers. The method can be generalized to investigate the deformed neutron structure of other odd-A nuclei.

In this part, we further investigate the neutron density distribution of ^{133}Cs by the deformed PVES model. The neutron

structure of ^{133}Cs has been investigated by using the coherent elastic neutrino-nucleus scattering data of the COHERENT experiment [50,51]. The authors determined the neutron radius by assuming a spherical neutron density distribution. In Fig. 8, we plot the deformed neutron density and weak charge density multipoles of ^{133}Cs calculated by the deformed RMF model. The weak charge density distributions $\rho_W(r)$ from the spherical RMF model are also shown in the same figure. The FSU parameter set is used. Additionally, the inset depicts the profile of the quadrupole density $\rho_{W2}(r)P_2(\cos\theta)$ in Eq. (5). In the deformed RMF calculations, ^{133}Cs has a prolate shape with the deformations $\beta_2^n = 0.106$ for $\rho_n(\mathbf{r})$ and $\beta_2^p = 0.114$ for $\rho_p(\mathbf{r})$, respectively. It corresponds to the positive values in the z direction and negative values in the x direction of the quadrupole density profile. The angular momentum of ^{133}Cs is $J^\pi = 7/2^+$, and higher Coulomb (weak) multipole form factors, which arise from the deformed density parts, should be included in the deformed PVES model.

With the spherical and deformed density distributions shown in Fig. 8(b), the A_{PV} results of ^{133}Cs are calculated and shown in Fig. 9. Similarly to the studies of ^{27}Al , we present the calculations from the deformed PVES model with and without the quadrupole neutron density ρ_{n2} . Comparing with ^{27}Al , ^{133}Cs has more obvious Coulomb distortion effects, larger isospin asymmetry, and smaller nuclear deformation. At the first diffraction minimum ($\theta \approx 4^\circ$), theoretical calcula-


 FIG. 9. Same as Fig. 4, but for ^{133}Cs at the beam energy of 2180 MeV.

tions are indistinguishable. However, there are discrepancies at the second diffraction minimum ($\theta \approx 7^\circ$). Compared with the spherical one, the deformed PVES model without ρ_{n2} provides a lower diffraction minimum, while it yields a larger diffraction minimum with ρ_{n2} . It is consistent with the results of ^{27}Al and is attributed to the differences between proton and neutron densities.

IV. SUMMARY AND CONCLUSIONS

In summary, we investigate the parity-violating asymmetry A_{PV} in a deformed scheme that combines the axially deformed RMF model and the DWBA method. By comparing the results with those obtained from the spherical PVES model, we examined how nuclear deformations, especially the neutron one, can impact A_{PV} results. To this end, we discussed the contributions of different multipole form factors and compare the A_{PV} calculations with and without neutron deformations.

We first calculated the parity-violating asymmetries for spherical nuclei ^{208}Pb and ^{48}Ca . The deformed PVES model can recover the results from the spherical PVES model and the calculations coincide with the measurements of PREX-II and CREX. Then we proceeded to investigate PVES of deformed nuclei ^{27}Al and ^{133}Cs . The deformed PVES model with and without neutron deformations yields larger and smaller diffraction minima, respectively, compared to the spherical

PVES model. This is because the quadrupole weak form factors, which are mainly provided by the quadrupole neutron density, have a significant influence on A_{PV} values near the diffraction minima. We propose that PVES can serve as a clear and model-independent method to fill the gap in knowledge of the neutron deformation, which has been less studied than the proton deformation. A more comprehensive understanding of the neutron deformation for odd- A nuclei is expected if A_{PV} can be measured near the diffraction minima. Our studies are helpful to gain a more complete picture of nuclear density distributions, which may play a potential role in the investigation of nuclear matter properties.

ACKNOWLEDGMENTS

This work is supported by the National Natural Science Foundation of China (Grants No. 12035011, No. 11975167, No. 11947211, No. 11905103, No. 11881240623, and No. 11961141003), by the National Key R&D Program of China (Contract No. 2018YFA0404403), by the Shandong Provincial Natural Science Foundation, China (Grant No. ZR2020MA096), by the Open Project of Guangxi Key Laboratory of Nuclear Physics and Nuclear Technology (Grant No. NLK2021-03), and by the Key Laboratory of High Precision Nuclear Spectroscopy, Institute of Modern Physics, Chinese Academy of Sciences (Grant No. IMPKFKT2021001).

-
- [1] R. González-Jiménez, J. A. Caballero, and T. W. Donnelly, *Phys. Rep.* **524**, 1 (2013).
 - [2] J. Erler, A. Kurylov, and M. J. Ramsey-Musolf, *Phys. Rev. D* **68**, 016006 (2003).
 - [3] D. Androić *et al.* (Q_{weak} Collaboration), *Nature (London)* **557**, 207 (2018).
 - [4] D. H. Beck and R. D. McKeown, *Annu. Rev. Nucl. Part. Sci.* **51**, 189 (2001).
 - [5] A. Acha *et al.* (HAPPEX Collaboration), *Phys. Rev. Lett.* **98**, 032301 (2007).
 - [6] Z. Ahmed *et al.* (HAPPEX Collaboration), *Phys. Rev. Lett.* **108**, 102001 (2012).
 - [7] T. W. Donnelly, J. Dubach, and I. Sick, *Nucl. Phys. A* **503**, 589 (1989).
 - [8] C. J. Horowitz, S. J. Pollock, P. A. Souder, and R. Michaels, *Phys. Rev. C* **63**, 025501 (2001).
 - [9] D. Adhikari *et al.* (PREX Collaboration), *Phys. Rev. Lett.* **126**, 172502 (2021).
 - [10] B. T. Reed, F. J. Fattoyev, C. J. Horowitz, and J. Piekarewicz, *Phys. Rev. Lett.* **126**, 172503 (2021).
 - [11] D. Adhikari *et al.* (CREX Collaboration), *Phys. Rev. Lett.* **129**, 042501 (2022).
 - [12] T. Dong, Y. Chu, Z. Ren, and Z. Wang, *Phys. Rev. C* **79**, 014317 (2009).
 - [13] J. Liu, C. Zhang, Z. Ren, and C. Xu, *Chin. Phys. C* **40**, 034101 (2016).
 - [14] C. J. Horowitz and J. Piekarewicz, *Phys. Rev. C* **64**, 062802(R) (2001).
 - [15] M. Centelles, X. Roca-Maza, X. Viñas, and M. Warda, *Phys. Rev. Lett.* **102**, 122502 (2009).
 - [16] J. Liu, Y. Wang, Y. Gao, P. Danielewicz, C. Xu, and Z. Ren, *Phys. Rev. C* **106**, 054605 (2022).
 - [17] T. Liang, Z. Ren, D. Bai, and J. Liu, *Phys. Rev. C* **106**, 054324 (2022).
 - [18] F. Wienholtz *et al.*, *Nature (London)* **498**, 346 (2013).
 - [19] F. J. Fattoyev, J. Piekarewicz, and C. J. Horowitz, *Phys. Rev. Lett.* **120**, 172702 (2018).
 - [20] M. Thiel, C. Sfienti, J. Piekarewicz, C. J. Horowitz, and M. Vanderhaeghen, *J. Phys. G: Nucl. Part. Phys.* **46**, 093003 (2019).
 - [21] G. Hagen *et al.*, *Nat. Phys.* **12**, 186 (2016).
 - [22] D. Androić *et al.* (Q_{weak} Collaboration), *Phys. Rev. Lett.* **128**, 132501 (2022).
 - [23] X. Roca-Maza, M. Centelles, X. Viñas, and M. Warda, *Phys. Rev. Lett.* **106**, 252501 (2011).
 - [24] J. Piekarewicz, A. R. Linero, P. Giuliani, and E. Chicken, *Phys. Rev. C* **94**, 034316 (2016).
 - [25] P.-G. Reinhard, X. Roca-Maza, and W. Nazarewicz, *Phys. Rev. Lett.* **129**, 232501 (2022).
 - [26] P. Sarriguren, M. K. Gaidarov, E. M. de Guerra, and A. N. Antonov, *Phys. Rev. C* **76**, 044322 (2007).
 - [27] N. Tsunoda, T. Otsuka, K. Takayanagi, N. Shimizu, T. Suzuki, Y. Utsuno, S. Yoshida, and H. Ueno, *Nature (London)* **587**, 66 (2020).
 - [28] Q. Y. Shou, Y. G. Ma, P. Sorensen, A. H. Tang, F. Videbaek, and H. Wang, *Phys. Lett. B* **749**, 215 (2015).

- [29] C. J. Horowitz *et al.*, *J. Phys. G: Nucl. Part. Phys.* **46**, 083001 (2019).
- [30] Y. Kanada-En'yo and H. Horiuchi, *Phys. Rev. C* **55**, 2860 (1997).
- [31] Y. Kanada-En'yo, *Phys. Rev. C* **71**, 014310 (2005).
- [32] J. N. Knudson *et al.*, *Phys. Rev. Lett.* **66**, 1026 (1991).
- [33] C. J. Horowitz, *Phys. Rev. C* **89**, 045503 (2014).
- [34] C. J. Horowitz, *Phys. Rev. C* **57**, 3430 (1998).
- [35] J. Liu, Z. Ren, T. Dong, and Z. Sheng, *Phys. Rev. C* **84**, 064305 (2011).
- [36] B. G. Todd-Rutel and J. Piekarewicz, *Phys. Rev. Lett.* **95**, 122501 (2005).
- [37] T. de Forest Jr. and J. D. Walecka, *Adv. Phys.* **15**, 1 (1966).
- [38] T. Liang, J. Liu, Z. Ren, C. Xu, and S. Wang, *Phys. Rev. C* **98**, 044310 (2018).
- [39] J. Liu, C. Xu, S. Wang, and Z. Ren, *Phys. Rev. C* **96**, 034314 (2017).
- [40] X. Li, Y. Wang, X. Guo, M. Chen, J. Liu, and C. Xu, *Chin. Phys. C* **46**, 014104 (2022).
- [41] J. Liu, C. Xu, and Z. Ren, *Phys. Rev. C* **95**, 044318 (2017).
- [42] P. P. Singhal, A. Watt, and R. R. Whitehead, *J. Phys. G: Nucl. Phys.* **8**, 1059 (1982).
- [43] L. Wang, J. Liu, T. Liang, Z. Ren, C. Xu, and S. Wang, *J. Phys. G: Nucl. Part. Phys.* **47**, 025105 (2020).
- [44] J. Liu, X. Liu, X. Wang, S. Wang, C. Xu, and Z. Ren, *J. Phys. G: Nucl. Part. Phys.* **48**, 125105 (2021).
- [45] O. Moreno, P. Sarriguren, E. Moya de Guerra, J. M. Udias, T. W. Donnelly, and I. Sick, *Nucl. Phys. A* **828**, 306 (2009).
- [46] W. Horiuchi and T. Inakura, *Prog. Theor. Exp. Phys.* **2021**, 103D02 (2021).
- [47] Y. Sugahara and H. Toki, *Nucl. Phys. A* **579**, 557 (1994).
- [48] A. Bohr and B. Mottelson, *Nuclear Structure Vol. 2: Nuclear Deformations* (World Scientific, Singapore, 1998).
- [49] T. Werner, J. Dobaczewski, M. Guidry, W. Nazarewicz, and J. Sheikh, *Nucl. Phys. A* **578**, 1 (1994).
- [50] D. Akimov *et al.*, *Science* **357**, 1123 (2017).
- [51] M. Cadeddu, C. Giunti, Y. F. Li, and Y. Y. Zhang, *Phys. Rev. Lett.* **120**, 072501 (2018).